Available online at www.sciencedirect.com
SCIENCE DIRECT®
International Journal of Heat and Fluid Flow 26 (2005) 45–55
International Journal of HEAT AND FLUID FLOW
www.elsevier.com/locate/ijhff

Natural convection flow structures and heat transfer in a model hydrothermal growth reactor

Hongmin Li [a], Minel J. Braun [a,*], Edward A. Evans [b], G.-X. Wang [a], Govind Paudel [a], Jason Miller [a]

[a] Department of Mechanical Engineering, University of Akron, Akron, OH 44325, USA
[b] Department of Chemical engineering, University of Akron, Akron, OH 44325, USA

Received 21 February 2004; accepted 21 June 2004
Available online 16 September 2004

Abstract

Due to the experimental difficulties brought about by high pressure and temperature growth conditions, flow and heat transfer in industrial hydrothermal autoclaves for the growth of single quartz crystals have been studied mostly numerically. To date, most of the numerical models and associated results are not experimentally validated; only qualitative validation data from experiments done during actual crystal growth production is partly available. In this study, the authors used a model simulated reactor represented by an enclosure with two lower half sidewalls uniformly heated while the upper half sidewalls are uniformly cooled. Flow structures in the reactor are qualitatively visualized using full field flow tracking; particle image velocimetry (PIV) is used for quantitative velocity pattern evaluation. Based on the physical setup and experimentally determined boundary conditions, flow is numerically simulated and the corresponding model is validated through comparison to the experimental results. The ensuing parametric studies show the changing of flow patterns and velocity magnitudes for a variety of enclosure aspect ratios.

Keywords: Natural convection; Flow visualization; Crystal growth; Enclosure

1. Introduction

Hydrothermal growth is currently the industrial method of preference to obtaining high quality piezoelectric single crystals (Byrappa, 1994; Buisson and Arnaud, 1994). The growth mechanism provides for low quality raw material pellets to dissolve under specified pressure and temperature conditions into a solution and generate, by nutrient deposition on special seeds (Laudise and Nielsen, 1961), high quality single crystals. The growth process is carried out in hydrothermal autoclaves where the raw material is located in a lower chamber, while seeds are hung in a connecting upper one (Laudise, 1970). Fluid super-saturation differences caused by a temperature differential and the ensuing natural convection process drive the solute nutrient material around the seeds and cause their growth (Klipov and Shmakov, 1991). Industrial growth practice shows that the nature and patterns of solution flow in autoclaves are critical to the quality, growth uniformity, and growth rates of the synthetic crystals (Klipov and Shmakov, 1991; Reid, 2003). Due to the difficulties encountered experimentally at high-temperature and especially high-pressure growth conditions (100–200 MPa, 350–450 °C), the flow of solution in industrial hydrothermal autoclaves is studied mainly numerically

* Corresponding author. Tel.: +1 330 972 7734; fax: +1 330 972 6027.
E-mail address: mjbraun@uakron.edu (M.J. Braun).

0142-727X/$ - see front matter © 2004 Elsevier Inc. All rights reserved.
doi:10.1016/j.ijheatfluidflow.2004.06.005

Nomenclature

A	surface area of the two lower (or two upper) heat exchangers	Ra_W	Rayleigh number based on enclosure width
g	gravity	W	width of the chamber
H	height of the enclosure	ΔT	temperature difference between lower and upper heaters
L	height of the heater exchanger		
Nu_L	Nusselt number based on heater height	*Greeks*	
Q	total heat transfer rate between upper and lower heaters	α	total heat transfer coefficient
		β	thermal expansion coefficient
Ra_L	Rayleigh number based on heater height	v	fluid kinematic viscosity

and then used in a predictive and extrapolating mode (Roux et al., 1994; Chen et al., 1999; Li et al., 2002, 2003). However, many of the numerical models used to date are not validated by experimental data and thus their predictions may not be reliable in setting or scaling up an autoclave based crystal growth process. Most common enclosure geometries provide for (i) the opposite side walls to be heated and respectively cooled and (ii) the bottom wall to be heated while the top one is cooled (Braun et al., in press). Flows in a cylindrical enclosure were studied as well for the thermosyphons. Lighthill (1953) solved theoretically the natural convection flow equations with a two-dimensional laminar model. In his model there is no fluid transport across the median plane and heat transfer from the lower to the upper half occurs by conduction only. Japikse and Winter's (1970) model is also a laminar one. They studied the transport mechanism at the mid-height plane and visualized the ensuing three-dimensional flow. Mallinson et al. (1981) studied the three dimensional flow in a rectangular enclosure when the flow was laminar and steady. All studies mentioned above have been conducted in the steady laminar flow regime. Experimental flow visualization and heat transfer studies where the lower half of the enclosure is hot and upper half is cold under unsteady laminar and/or transition regimes have not been documented in the literature to date.

2. Scope of work

In this paper we shall investigate the flow in unsteady laminar and/or transition regimes and visualize the flow qualitatively using quantitative information generated by a full flow field visualization method. An experimental device is set up to model realistically the flow in hydrothermal autoclaves. Besides gaining information regarding flow in such environments, these experiments are used to provide initial and boundary conditions to a numerical model that is used first in a validating and then in a predictive mode.

3. The experimental facility

3.1. The system facility

A schematic of the experimental system is shown in Fig. 1. The system contains a test section connected to a set of constant temperature circulating baths. The two separate water baths supply constant high temperature water at $T_H = 35\,^{\circ}C$ to the two lower-half heaters and constant low temperature water at $T_L = 25\,^{\circ}C$ to the two upper-half heaters, respectively. For each pair of heaters, water flow rates are kept the same by using connecting tube networks with similar flow resistance. The same flow rate in the lower- and upper-half heaters set up a symmetric heating pattern for the fluid in the test enclosure. Uniform temperatures on the heater surfaces are achieved by keeping large water flow rates through the heaters in order to minimize the temperature rise in the heating (cooling) agent. The laser and camera section includes a laser as a light source, a group of lenses, and a high-resolution video camera that images the flow. The data acquisition and image processing section reads the temperatures from the thermocouples, acquires and stores images from the video camera, and generates both quantitative flow velocity and temperature data.

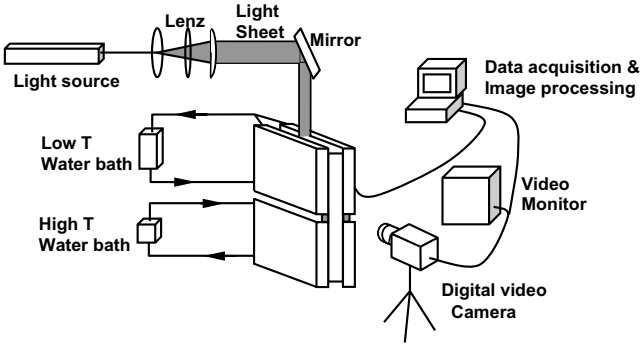

Fig. 1. Schematic of the experimental system.

3.2. The laser and vision system

Various embodiments of the visualization system used in these experiments have been described previously in great detail (Braun et al., 1990a, b). The system, Fig. 1, contains a high-power, 5 W, Argon-Ion continuous wave laser, a combination of cylindrical lenses that transform the cylindrical beam of light into a coherent light sheet that is approximately 0.020 in. (0.5 mm) thick, and an image recording system. The fluid is seeded with 5–20 μm magnesium oxide particles. A modified digital Pulnix camera allows either interlaced or non-interlaced viewing of the illuminated plane in the fluid, at a frequency of 30 Hz, which is the NTSC standard image sampling frequency. The camera-lens system has been configured as a long distance microscope (LDM), thus simultaneously allowing both a large working distance (10–25 in./254–635 mm) and high magnification (up to ×400). The laser, while not synchronized with the camera, was used in either an externally strobed mode at frequencies that were even multiples (120, 240 Hz) of those of the camera, or a non-strobed mode. The digital video camera, which is focused on the plane of the light sheet, obtains continuous videos, or snapshot images of the tracing particles. Videos and images from the camera are transferred into a PC, RAM based data acquisition system (and to an analog tape) and computer-processed to obtain the velocity data.

For the visualization of the temperature field we are using Thermochromic Liquid Crystals (TLC) as seeding particles. These almost-neutrally buoyant encapsulated particles have the property of changing colors with temperature and are best illuminated with a Xenon white light-sheet source. The crystals are designed to be active for a certain temperature range and the colors change continuously across the spectrum from red (cold) to blue (hot). The narrower the temperature range is, the higher the resolution of the color/temperature bands become.

The qualitative fluid flow patterns and associated quantitative velocity fields were visualized using magnesium oxide micro-particles illuminated by the laser source described above. The usage of these particles ensured a high resolution of pattern visualization and allowed the particle velocimetry software to determine with a high degree of precision the local flow velocities, both in the wall layers and the central core.

3.3. The test section

The configuration of the test section is shown in Fig. 2. The central section is a Plexiglass box, 368 mm high, 216 mm wide, and 89 mm thick. The wall thickness is 13 mm. The inside surfaces of the bottom and back walls are painted flat black in order to eliminate light reflection and glare into the camera lens. The test box is sandwiched between two separate sets (of two heaters each)

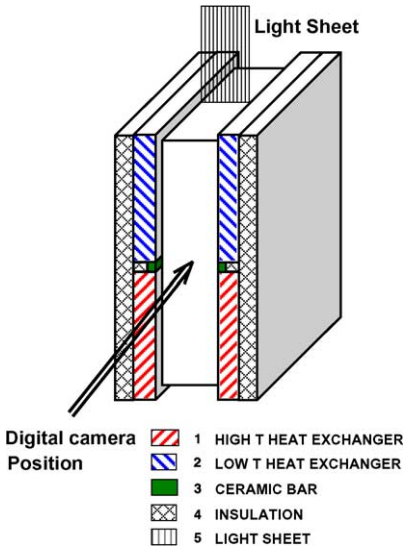

Fig. 2. Schematic of the test section.

of flat surface heat exchangers (HE) that provide the driving temperature differentials for the test fluid. The upper section is formed by two parallel and opposite low temperature HEs, while the lower section contains two similarly placed high temperature HEs. The HEs are insulated on their air-exposed side to reduce heat loss to the environment. In order to monitor temperatures of the test liquid/HE surface interface, flat wire thermocouples (1.57E−4 mm thick) were installed, as shown in Fig. 3. On the left hand side there are eight thermocouples arranged in a vertical formation along the centerline to check vertical temperature uniformity. Thermocouples 9, 10 and 11, 12 respectively, are measuring the horizontal temperature uniformity, while thermocouples 13 and 14 are mounted at mirror locations, to 3 and 6, on the right side HEs. This arrangement has been chosen to confirm that the two upper HEs and two lower HEs provide symmetrical heating.

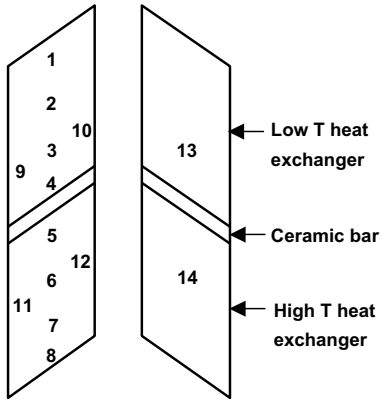

Fig. 3. Locations of thermocouples on the heat exchanger surfaces.

4. Numerical models

For purpose of comparison, we shall present both, two and three-dimensional models for flow pattern simulation. Thus, Fig. 4a presents the two-dimensional (2-D) physical embodiment while, Fig. 4b presents the three-dimensional (3-D) one. Fig. 4c, details the location of the vertical cross sectional plane $Z0$ in which experimental and numerical results will be later presented. In both models every surface that represents a boundary to the fluid domain is lettered as shown in Table 1(a) and (b) respectively. The temperature boundaries on the HE surfaces are assumed to be uniform and the temperatures measured by the thermocouples are used to establish the thermal levels of these boundaries. Due to their low thermal conductivity, the top and bottom walls of the Plexiglass box, ((ab) and (gh) for the 2-D model, and ABB′A′ and GHH′G′ for the 3-D model), are considered to be adiabatic. Further, for the 3-D model, the vertical enclosure walls, ABHG and A′B′H′G′ are considered to be adiabatic. For both the 2-D and 3-D models, the full Navier–Stokes and energy equations are solved interactively in a feedback mode. Whether 2-D, or 3-D, in vector format the governing equations are given by Eqs. (1)–(3).

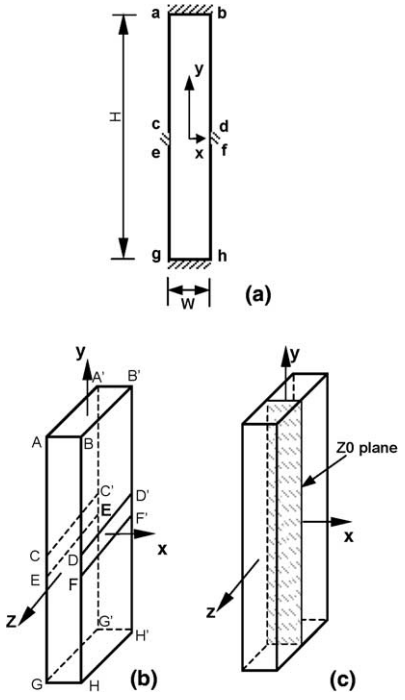

Fig. 4. Schematic of the domain and boundaries for the numerical models: (a) the 2-D model, (b) the 3-D model, (c) visualization plane in the 3-D model.

$$\nabla \vec{U} = 0 \tag{1}$$

$$\frac{\partial \vec{U}}{\partial t} + \vec{U} \cdot \nabla \vec{U} = -\frac{1}{\rho} \operatorname{grad} P + \nu \nabla^2 \vec{U} + \vec{F} \tag{2}$$

$$\frac{\partial T}{\partial t} + \vec{U} \cdot \nabla T = \frac{k}{\rho \cdot Cp} \nabla^2 T \tag{3}$$

where the velocity vector is $\vec{U} = [u\ v]$ for the two-dimensional model and $\vec{U} = [u\ v\ w]$ for the three-dimensional one, respectively. The buoyancy force, $\vec{F} = g \cdot \beta \cdot (T - T_0)$, is oriented in the positive y direction due to the choice of coordinate system. In this study, T_0 is introduced as a reference temperature and is set to the average value between $T_H = 25\,^{\circ}C$ and $T_L = 35\,^{\circ}C$. The above equations are solved for the geometry shown in Fig. 4a and b, and the boundary conditions listed in Table 1(a) and (b), respectively. The working fluid is water with physical properties measured at 30 °C and 1 atm.

The numerical solution uses a commercial CFD package, FLUENT, which employs a finite volume method for the discretization of the continuity, momentum and energy equations. Also for the momentum equations, a second order upwind scheme is used. The unsteady flow time-marching employs the second order implicit scheme and a time step of 0.05 s. The size of the time step is chosen based on the total computing

Table 1
Panel (a): Boundary conditions for surfaces shown in Fig. 4a. Panel (b): Boundary conditions for surfaces shown in Fig. 4b

Location	Surface	Type
Panel (a)		
Top and bottom	ab, gh	Adiabatic wall
Upper heaters	ac, bd	Wall at T_L
Lower heaters	eg, fh	Wall at T_H
Wall between heaters	ce, df	Adiabatic wall
Panel (b)		
Top and bottom	ABB′A′, GHH′G′	Adiabatic wall
Front and back	ABHG, A′B′H′G′	Adiabatic wall
Upper heaters	AA′C′C, BB′D′D	Wall at T_L
Wall between heaters	CC′E′E, DD′F′F	Adiabatic wall
Lower heaters	EE′G′G, FF′H′H	Wall at T_H

time needed to simulate the flow for a period of flow time, since a larger time step needs more iterations for each time step. On the other hand, the numerical results are not sensitive to the time step size at around 0.05 s (0.01–0.1 s). The residuals of continuity, momentum, and energy equations are required to be below 10^{-6}, 10^{-4}, and 10^{-6} respectively, for each time-step convergence. The under-relaxation factors for mass, momentum, and energy are set to 0.2, 0.5, and 0.8 respectively. Note that with water as the working fluid, and based on the enclosure thickness, W, (common for both the 2-D and 3-D models), the Rayleigh number, $Ra_W = \frac{g\cdot\beta\cdot\Delta T\cdot W^3}{\nu^2} Pr = Gr \cdot Pr$, equals 1.77×10^8 which indicates either unsteady laminar, or transitional flow.

To increase the level of confidence in the numerical results, grid convergence studies were performed for both the 2-D and 3-D models. The measure by which we judged results convergence has been the time averaged heat flux Q, transferred to the fluid from the two lower HEs together with the magnitude and period of the fluctuating temperature at the center of the enclosure. These indicators were chosen simply because they represent the end-results that incorporate the effects of all other dependent variables at work: $\vec{U}, P, \vec{F}$, and the heat transfer coefficient. An inspection of Table 2 reveals that for both the 2-D and 3-D cases, grids #3 present a difference in the averaged heat flow Q from grids #2 of only 1.2% and 2.5% respectively. The difference in the "Averaged Q" is now much smaller than the difference when grids #1 and grids #2 were compared. Further grid size reduction becomes prohibitive when one weighs the change in "Average Q" against the computational time required to achieve even higher resolution with no added physical insight. Temperature fluctuation convergence difference between grid #2 and grid #3 is also below 2%. Thus, for the purpose of this study, and taking into consideration as the CPU time expended in the respective computations, the authors felt that the results presented with the configurations of grid(s) #3 are acceptably converged. All results and discussions that follow are based on the results of "grid(s) #3".

5. Results and discussion

5.1. Heat exchanger surface temperatures

As mentioned in the description of the test section, the side heater walls are arranged in a symmetric fashion with respect to the sides of the Plexiglass box. The temperature measurements on the heater surfaces at the points shown in Fig. 3, support well the previous statement and show the temperature uniformity on the heat exchanger surfaces. The temperature readings of the thermocouples are actually the numbers that are used as temperature boundary conditions inputs for the numerical models. The horizontal uniformity of the wall temperatures and its symmetric quality are also excellent. The high quality performance of these heat exchangers not only ensured a well-controlled experiment, but also helped in obtaining a valid comparison with the numerical results.

5.2. Three-dimensional numerically generated flow structures

The flow structures corresponding to the HEs surface temperature difference ($\Delta T = 10\,^{\circ}\mathrm{C}$) are presented in Fig. 5a and b. Fig. 5a presents numerically simulated flow patterns in the symmetry plane $Z0$ (Fig. 4), while Fig. 5b presents the corresponding composite of the experimentally obtained flow vectors. The results stem from the exercise of the FLUENT three-dimensional model. On inspection of both figures, one can notice the coincidence of the major flow formations and of the locations at which they occur. Thus, on the two upper heaters, the wall layers are moving downward, while the two lower HE surfaces generate similar but upward moving wall layers. This situation creates two flow regions that are on a "head-on" collision path in the vertical median region of the enclosure. This region, clearly visible in Fig. 5, contains upper and respectively lower recirculation zones located in an anti-symmetric position and occupying most of the their corresponding halves of the enclosure. The strong central vortex alone,

Table 2
Grid independence obtained for the 2-D simulations and 3-D simulations

	Grid #1	Grid #2	Grid #3
Panel (a)			
2-D grid density			
No. of cells (XY)	50×150	100×300	200×600
Averaged Q (J/s)	$Q1 = 60.93$	$Q2 = 64.51$	$Q3 = 65.29$
(% Change)/100		$(Q2 - Q1)/Q1 = 0.058793$	$(Q3 - Q2)/Q2 = 0.012085$
Panel (b)			
3-D grid density			
No. of cells (XYZ)	$40 \times 30 \times 80$	$60 \times 40 \times 120$	$90 \times 60 \times 180$
Averaged Q (J/s)	$Q1 = 66.37$	$Q2 = 71.56$	$Q3 = 73.36$
(% rate of change)/100		$(Q2 - Q1)/Q1 = 0.0794$	$(Q3 - Q2)/Q2 = 0.0251$

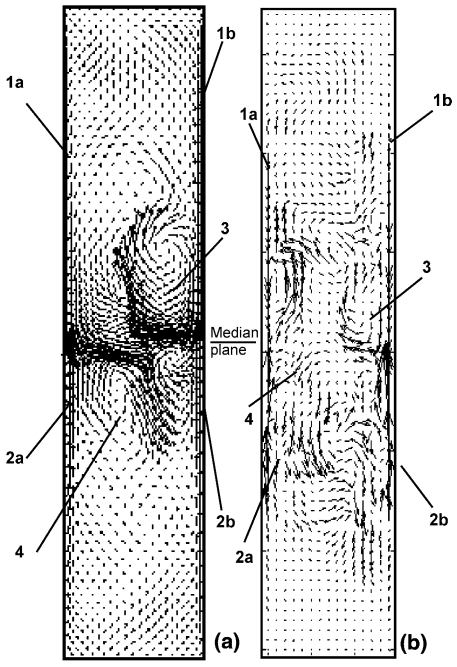

Fig. 5. Flow structure in $Z0$ plane in the enclosure with $\Delta T = 10\,^{\circ}C$: (a) 3-D numerical model (Plane $Z0$), (b) Experiment. 1a, 1b—downward moving wall layers, 2a, 2b—upward moving wall layers, 3, 4—vortical regions.

occupies almost 1/3 of these zones. Details of both the numerical and experimental nature of the central zones are shown in Fig. 6a and b. In the enlarged vector plots of Fig. 6a, one can see the flow streams formed by the wall layers. It was visually observed that the streams' behavior in this central region is unsteady and cyclical in nature. They were continuously changing their directions, with the caveat that these changes were contained in an envelope, and thus the overall nature of the flow presented in the time snapshots of Fig. 5b and Fig. 6b are totally representative of the nature of the flow averaged over time. When compared with the fluctuating streams described heretofore, the wall layers themselves are quite steady and do not change directions. Fluid mixing in the wall layers is weak and very limited in extent. Comparatively, mixing in the central region of the enclosure is strong due to the unsteady flow streams. Based on experimental observation, the overall unsteadiness of the flow in the enclosure seems to be caused by the "head-on" collision of the up-flowing and down-flowing wall layers since flow is steady before the collision (in the wall layers), and streams formed by wall layer flows, become unsteady after the collision.

5.3. Quantitative comparison between experimental and numerical data

Fig. 7 presents, the superimposed-experimental velocity data in the wall layers and numerical data in the near wall region at two height locations in the $Z0$ plane. One location is at a distance of $1W$ above the median plane and the second location is at $2W$ above the median plane (W is the width of the enclosure). As described above, flows are steady in the wall layers and unsteady in the central region. Fig. 7a, presents a magnified detail of the experimentally visualized boundary layer and the immediate adjacent region. Comparison between the numerical and experimental data is limited to the wall layers. The four wall layers (1a, 2a, 1b, 2b, Fig. 6a) are the main driving force of the flow in the enclosure. From the study of Fig. 7, it can be seen that there is good agreement between the experimental and numeri-

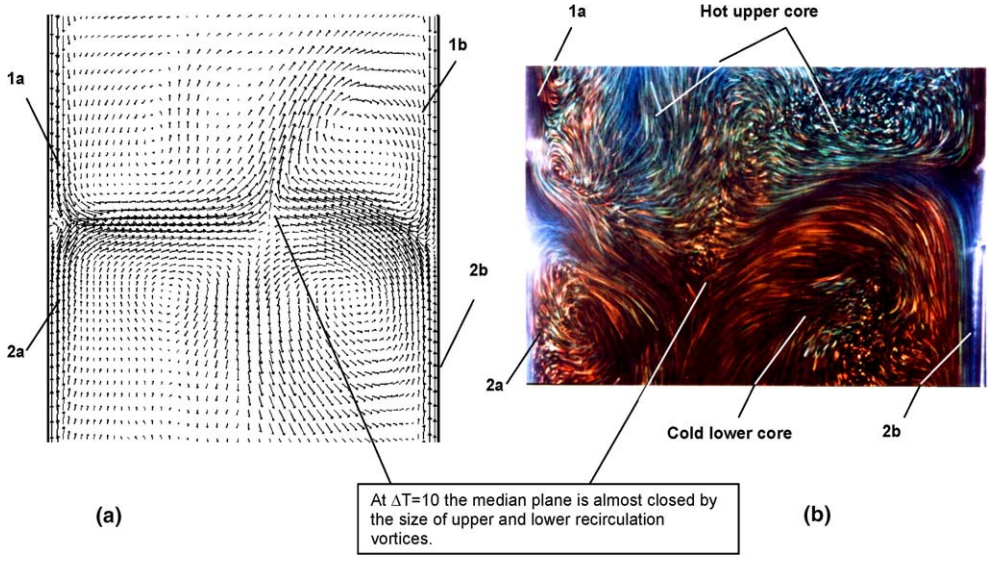

Fig. 6. Detailed view of the wall layers and core vortices in the central zone of the enclosure: (a) results of the numerical 3-D model, (b) photo of flow taken with exposure time one second. Color shown by liquid crystal particles.

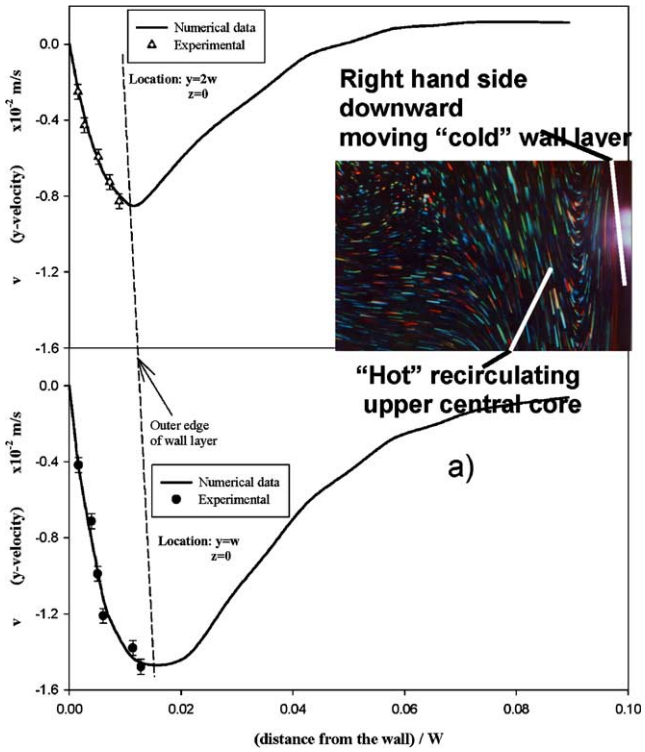

Fig. 7. Velocities in the downward wall layers and comparison between numerical and experimental data. (Color photo shows the cold, downward moving boundary layer and the immediate adjacent hot core).

cal data for the boundary layer velocity. Further comparison to Fig. 7a reveals also good overall qualitative agreement with the velocity fields of Fig. 5.

5.4. Temperature distribution in the enclosure

The temperature distributions presented herein were obtained with the same 3-D thermo-fluid numerical model used for the determination of the velocity fields. Just like for the velocities discussion, the temperature patterns, Fig. 8, are presented in the $Z0$ plane at the same two height locations used in Fig. 7 plus the corresponding symmetrical locations below the median plane. One can see from Fig. 8, as well as from Fig. 6b (temperature levels indicated by liquid crystal color) that while the temperature in the central regions is quite uniform, large temperature gradients exist in the wall layers. The flow in the wall layer appears to be steady and two-dimensional (with no heat transfer and mixing in the Z direction) with the heat transfer mechanism across the wall layers controlled by molecular diffusion. As mentioned, in the central region, flow is unsteady and eminently three-dimensional. Heat transfer and mixing in the central region is much more effective than the diffusion process in the wall layer. The former, which occupies about 90% of the space in the enclosure, exhibits a rather uniform temperature; thus these regions act as

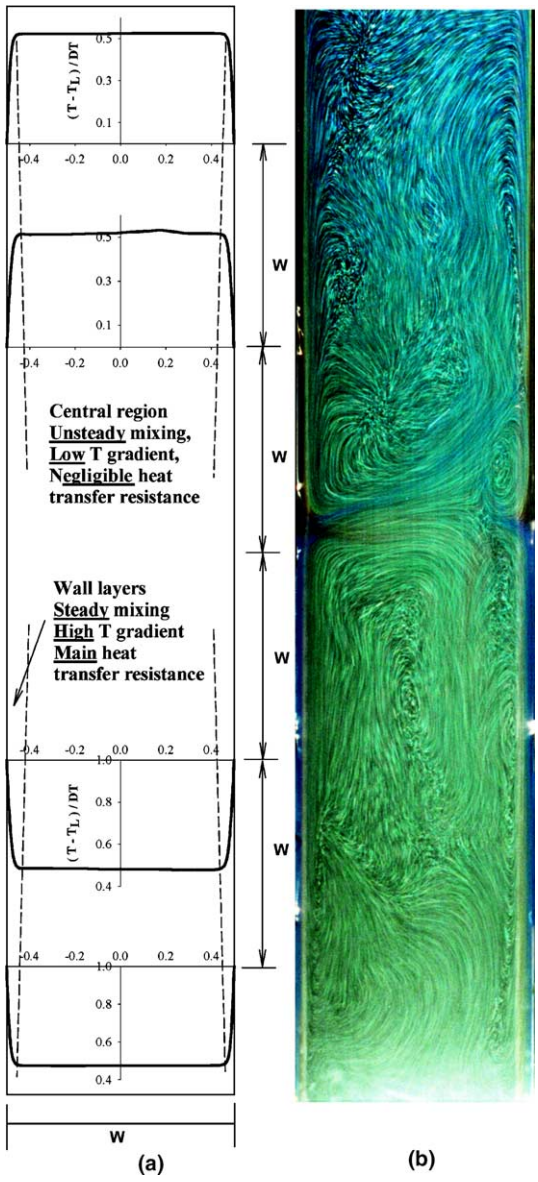

Fig. 8. Temperature across the enclosure, wall layers and the central region: (a) obtained with the 3-D model and $\Delta T = 10\,^{\circ}\mathrm{C}$, (b) experimental photo with color shown by liquid crystal particles.

heat reservoirs that supply heat to, (in the upper half) or receive heat from (in the lower half) the wall layers.

The use of the liquid crystals for temperature evaluations used in the context of this paper is only qualitative in nature. The liquid crystals have a range width of 4 °C, during which they change color from red (28 °C) to blue (32 °C) going through all colors of the spectrum. As one can see from Fig. 6b, Fig. 7a and Fig. 8b, the hot and cold temperatures regions are shown clearly by the changes in colors.

It is notable that the average temperature in the central region of the upper half, as plotted in Fig. 8a, and shown by the liquid crystals in Fig. 8b is higher than the average temperature of the lower reservoir. At the same time the wall layers in the lower half have a higher

temperature (mostly blue in color) than the central core (reddish in color), while the situation is reversed in the upper half. This distribution of temperatures appears somewhat counterintuitive at first, but judged in the context of the flow patterns exhibited by Figs. 5 and 6a is completely justified. Thus, one can see that the hot wall layers generated in the bottom half are driven by buoyancy upward and across the middle section filling the upper central core with hot fluid; the opposite process takes places with the cold wall layers borne along the surfaces of the upper, colder heat exchangers walls. They too, cross the middle section into the lower central core and fill it with the colder fluid. This process continues uninterrupted with the wall layers acting in a steady manner while the mixing in the central cores is highly periodic. This periodicity in itself is the actual engine of the "push–pull" phenomenon that takes place in the central core region between the lower- and the upper-halves. One must emphasize that the flow repeats itself qualitatively, but the size of the structures changes between cycles.

5.5. The 2-D simulation and comparison with the 3-D results

The two-dimensional model assumptions are displayed in Table 1(a). They are identical (for the corresponding faces) to the boundary conditions used in the three-dimensional simulation, as shown in Table 1(b). Fig. 9a and b show on a comparative basis the flow patterns resulting from the exercise of the 2-D, FLUENT model, and the 3-D flow model respectively (see also Fig. 6a (plane $Z0$)). This case-study is for a $\Delta T = 10\,^{\circ}\mathrm{C}$. On inspection, it can be seen that the two models result in the same overall flow patterns. Thus, one can observe the formation of the same wall layers on each of the HE walls, as well as similar respective recirculation zones associated with the central stream flow in the lower- and upper-half respectively. The main difference though, resides in the strength and size of the recirculation vortices as well as the resulting "communication channel" between the lower and upper halves. As already discussed in the 3-D case, the circulation between the lower- and upper-half is interdicted by the size (width) of the respective recirculation zones, a fact that results in a redirection of the flow in the third direction (Z). In the 2-D case the third direction is missing, thus forcing the flow to move exclusively in an (X–Y) plane. Consequently, the recirculation vortical zones are narrower, but oblong, and there is strong communication between the lower and upper half.

Since in the 2-D model contribution to mixing in the Z direction is neglected, it becomes evident that the unsteady 3-D flow would cause stronger mixing in the median enclosure region than the one predicted by the 2-D model. Correspondingly, the 2-D model prediction

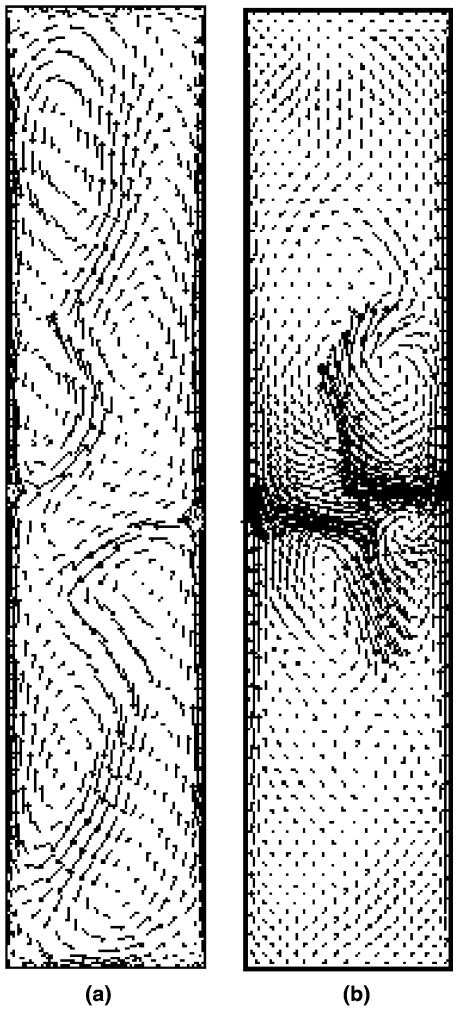

Fig. 9. Comparison of flow profiles obtained with the numerical (a) 2-D and (b) 3-D models.

of the total heat transfer rate from the two lower heaters to the two upper heaters is lower than that of the 3-D model by approximately 11%, as can be seen from a comparison of the "Average Q" between Table 2(a) and (b).

As a partial conclusion, we can state that the 3-D effect is important and neglecting flow in the Z direction makes the 2-D model prediction only an approximation to the real flow. However, when comparing the overall effect of the heat transfer in the enclosure, the prediction by the two-dimensional model is only 11% lower than the three-dimensional simulation. Considering the prohibitive computing time required by the 3-D cases, 2-D models can still be used to obtain a reliable guiding first approximation.

5.6. Numerical parametric study

The 3-D numerical model was validated by our experimental data, and the comparison with the 2-D model showed that one can rely on the latter for predictions

underlying the 3-D true nature of the flow. As a consequence we shall proceed further with a numerical parametric study carried out with the 2-D model only.

The first parametric study varies the aspect ratio by keeping the height of the enclosure, H, constant while varying its width W. Fig. 10 presents the heat transfer coefficient α based on the total heater transfer area, $\alpha = \frac{Q}{A \cdot \Delta T}$, where A is the surface area of the two lower HEs. For this parametric study, ΔT is kept at 10 °C. The simulation plotted in Fig. 10 was checked for grid independency resulting in a choice of grid density of 100 (W) × 400 (H).

At low aspect ratio ($H/W < 10$), the heat transfer coefficient and the average heat flux based on the heater surface area change only slightly. Overall flow patterns show sepearate wall layers on each of the four HE surfaces. Compared with the width of the chamber, the thickness of the wall layers are still very small and do not interact with each other across the enclosure. The central stream traveling between the lower and the upper halves of the enclosure and the recirculation zones still occupy most of the chamber. As a result the resistance to heat transfer is encountered mainly in the wall layers. Fig. 11a shows the flow pattern for the aspect ratio $H/W = 2.4$. The flow patterns exhibited by this figure remain qualitatively the same as long as $H/W < 10$. The characteristic length for this configuration is the height of one heat exchanger, L.

As the aspect ratio increases past 10, ($10 < H/W < 20$), the boundary layers on the opposite walls start to interfere with each other near the median region. This interference changes significantly the heat exchange process between the heaters and the fluid. Since, as Fig 11b, c and d show, the stream separating the wall layers and convecting heat from the lower to the upper chamber is throttled more and more, the resistance to heat transfer increases in each one of the enclosure's halves. With it, the difference between the bulk fluid temperature and the wall temperature decreases as well. This situation is conducive to much smaller heat transfer coefficients as proved by the dramatic drop in the heat transfer coefficient, α, in Fig. 10 (segment (bcd) of the curve). In this range of aspect ratios, the heat transfer depends on both the width of the chamber and the height of the heaters. Thus an appropriate length scale is a combination of these two dimensions, something akin to a hydraulic diameter.

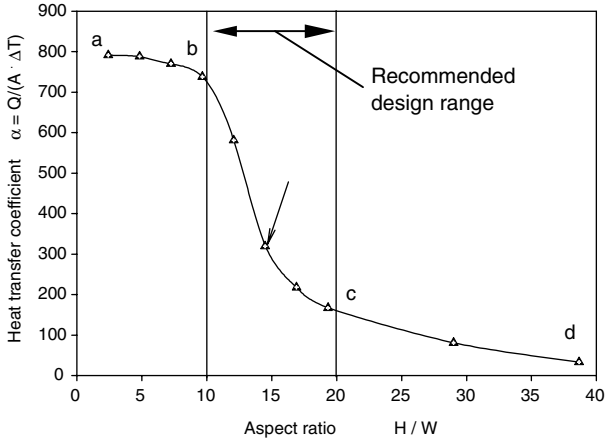

Fig. 10. Heat transfer coefficient for various aspect ratios with the enclosure height kept the same.

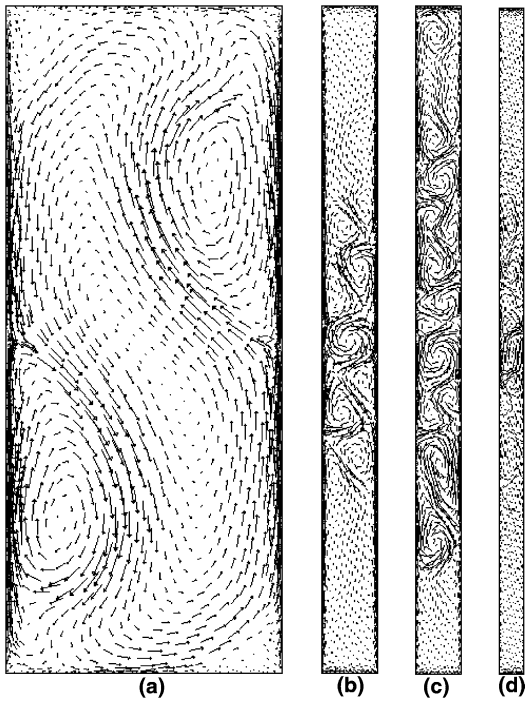

Fig. 11. Flow patterns with various aspect ratios: (a) aspect ratio = 2.4, (b) 12, (c) 14.5, (d) 29.

For aspect ratio $H/W = 12$, Fig. 11b shows that the recirculating flow cells start forming in the median section and are large enough to occupy the entire space between the wall layers. As a result, the communication between the lower and upper chambers is cut off and α drops from point (b) to (c), Fig. 10. As the aspect ratio continues to increase to $H/W = 14.4$, the number of recirculating flow cells increases as well, occupying almost the entire chamber, Fig. 11c.

Further increase in the aspect ratio $H/W > 20$ will lead to a different flow pattern in the chamber. The wall boundary layers on the four heater surfaces do not have the necessary space to properly develop before reaching the median section. The anti-symmetric flow pattern is replaced by a multi-cell pattern "only", located in the chamber median plane and the fluid away from it is almost in a state of stagnation. Heat transfer by convection across the horizontal median plane ceases completely. It is apparent that the heat transfer follows through a conduction process across the cross section (XZ plane). In this case the width of the chamber

becomes the characteristic length scale. Fig. 11d shows the flow pattern for aspect ratio $H/W = 29$.

Two issues are the most important for crystal growers and autoclave designers. The first requires the enclosure to have at least two temperature zones: for example, the simplest configuration will have the lower-half at higher temperature and the upper-half at a lower temperature. The second pertains to the fluid exchange rate and flow regime between the two halves since the fluid exchange is instrumental in the transport of the nutrient and the subsequent mass transfer. From Figs. 10 and 11, one can see that at a low aspect ratio ($H/W < 10$) the dominating temperature gradients (or heat transfer resistance) are at the wall. The center region is at a relative uniform temperature, which indicates that the two temperature zones are not yet established. At the high aspect ratio ($H/W > 20$) however, the fluid exchange between the two halves is blocked by the circulation zones at the median height. The aspect ratio range that can separate the temperature zones and at the same time can provide a fairly high fluid exchange rate is from $H/W = 10$–20. Thus, the combination of qualitative and quantitative knowledge yielded by Figs. 10 and 11 can give reactor designers solid guidance towards preferable geometric ratio ranges.

The second parametric study involves choosing three aspect ratios that are kept constants (2, 4.83, and 8 respectively), while changing parametrically the height H (or scale) of the enclosure. This particular choice of aspect ratio will help verify that, in this range, ($H/W < 10$), the hypothesis of having the height of the heat exchangers as the characteristic length scale is the correct one. The cases considered for this study are detailed in Table 3. For each aspect ratio, cases with various chamber heights are simulated with the previously validated numerical model. The non-dimensional parameters, Nu_L and Ra_L are plotted in Fig. 12. Nu_L is defined by $Nu_L = \frac{\alpha \cdot L}{k}$ where L is the height of the heat exchanger and k is the conductivity of the fluid. Correspondingly Ra_L is defined by $Ra_L = \frac{g \cdot \beta \cdot \Delta T \cdot L^3}{\nu^2} Pr$ where ΔT is the temperature difference between the upper heater and the lower heater surfaces and Pr is the Prandtl number of the fluid. One can see from the figure that the relation between Nu_L and Ra_L follows a smooth curve for all three aspect ratios, with no discontinuities. That gives credence to the correctness of our earlier assumption regarding the characteristic length for $H/W < 10$.

Table 3
Numerical parametric study for three different aspect ratios (H/W)

Aspect ratio	$H/W = 2$	4.833	8
Height of the chamber H, in meter	0.0516	0.0368	0.0663
	0.110	0.0737	0.147
	0.221	0.184	0.295
	0.516	0.368	0.663
	0.921	0.737	1.29
		1.47	

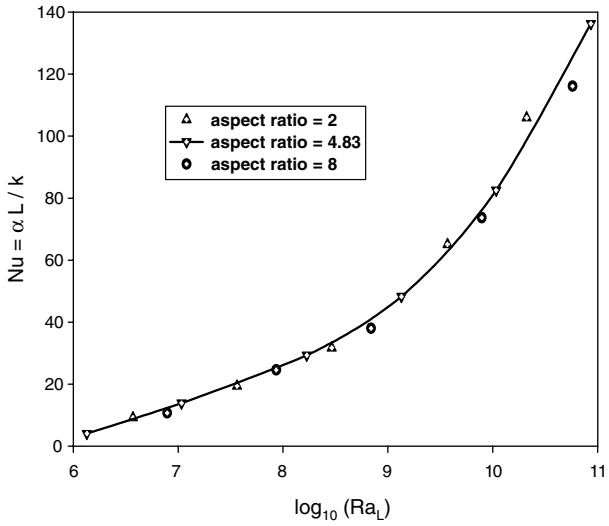

Fig. 12. Heat transfer in enclosures with aspect ratio less than 10.

6. Conclusions

Flows in an enclosure with two sidewalls differentially heated (lower part heated and upper part cooled) are studied experimentally and numerically. The three-dimensional flow structures numerically modeled agree well with the experimental results. It was found that the two-dimensional model predicts qualitatively the same overall flow pattern but with a lower total heat transfer rate because flow in the third direction is neglected. The main components of the flow are the wall layers, which represent the driving flow that causes recirculating vortical patterns, and cross-flows between the lower and upper cores of the enclosure. It was determined that for this physical configuration, with the height of the chamber being kept constant, when the aspect ratio is less than 10, the characteristic length is represented by the height of the heater. When the $10 < H/W < 20$, the characteristic length appears to change to a dimension that is akin to the hydraulic diameter and when $H/W > 20$, the width of the enclosure becomes the characteristic length. As the characteristic length changes, so does the nature of the flow and associated heat transfer in the chamber (Fig. 10). When the thickness of the wall layer is very small compared to the width of the chamber, convective effects dominate. If the boundary layers start to interfere with each other, flow communication between the lower and upper halves may cease, and eventually as H/W increases, conduction may become the preferred mode of heat transfer. Most importantly, it has to be noted that the nature of the flows is unsteady for the ΔT and Ra number chosen, and that cessation of flow circulation

between the lower and upper halves for $\Delta T = 10\,^{\circ}\mathrm{C}$ will be very unfavorable to the crystal growth process. These findings can be used directly by the autoclave designer in his quest for an environment that fosters favorable velocity and temperature gradients.

Acknowledgment

The authors would like to thank the College of Engineering at The University of Akron, Sawyer Research Products, and The National Science Foundation for their support.

References

Braun, M.J., Hendricks, R.C., Canacci, V., 1990a. Non-intrusive qualitative and quantitative flow characterization and bulk flow model for brush seals. In: Proceedings of the Japan International Tribology Conference, III, Nagoya, Japan, 1990, pp. 1611–1616.

Braun, M.J., Canacci, V.A., Russell, L.M., 1990b. Non-intrusive laser based computer aided high speed flow visualization in an air tunnel. In: Proceedings of The Fifth International Symposium on Application of Laser Techniques to Fluid Mechanics, Lisbon, Portugal, 1990, pp. 6.1–6.6.

Braun, M.J., Lattime, S.B., Moore, C.H., Choy, F.K., 1992. A computer based automated method for non-extensive temperature evaluation using thermochromic liquid crystals (TLC). In: The Sixth International Symposium on Applications of Laser Techniques to Fluid Mechanics, July 20–23, Lisbon, Portugal, pp. 3.5.1–3.5.6.

Buisson, X., Arnaud, R., 1994. Hydrothermal growth of quartz crystals in industry: present status and evolution. J. de. Physique IV 4 (Colloque C2, supplement au J. de Physique III), C2-25–32.

Byrappa, K., 1994. Hydrothermal growth of crystals. In: Hurle, D.T.J. (Ed.), Handbook of Crystal Growth. Elsevier Science B.V., North-Holland, pp. 465–562.

Chen, Q.S., Prasad, V., Chatterjee, A., Larkin, J., 1999. A porous media-based transport model for hydrothermal growth. J. Crystal Growth 198–199, 710–715.

Japikse, D., Winter, E.R.F., 1970. Heat transfer and fluid flow in the closed thermosyphon. Heat transfer 1970, 4th International Heat Transfer Conference, Paris-Versailles 1970, NC 2.9, pp. 1–11.

Klipov, V.A., Shmakov, N.N., 1991. Influence of convective flows on the growth of synthetic quartz crystals, In: Forty-Fifth Annual Symposium on Frequency Control, IEEE, pp. 29–36.

Laudise, R.A., 1970. The growth of single crystals. Prentice-Hall, Englewood Cliffs, NJ.

Laudise, R.A., Nielsen, J.W., 1961. Hydrothermal crystal growth. In: Seitz, F., Turnbull, D. (Eds.), Solid State Physics, 12. Academic Press, New York, pp. 149–222.

Li, H., Evans, E., Wang, G., 2002. Flow and heat transfer study in an autoclave for hydrothermal crystal growth with a three-dimensional conjugate heat transfer model. In: IMECE2002-33709, Proceedings of IMECE2002: 2002 ASME International Mechanical Engineering Congress & Exhibition, New Orleans, Louisiana, 2002.

Li, H., Evans, E.A., Wang, G.-X., 2003. Flow of solution in hydrothermal autoclaves with various aspect ratios. J. Crystal Growth 256 (1–2), 146–155.

Lighthill, M.J., 1953. Theoretical consideration on free convection in tubes. The quarterly Journal of Mechanics and Applied Mathematics 6 (part 4), 398–439.

Mallinson, G.D., Graham, A.D., de Vahl Davis, G., 1981. Three dimensional flow in a closed thermosyphon. Journal of fluid mechanics 109, 259–275.

Reid, J.B., 2003. Sawyer Research Products Inc., Personal communication.

Roux, B., Louchart, O., Terhmina, O., 1994. Hydrodynamic aspect of hydrothermal synthesis of quartz bulk flow regimes. J. de. Physique IV 4 (Colloque C2, supplement au J. de Physique III), C2-3–11.